

Dynamics of a driven harmonic oscillator coupled to independent Ising spins in random fieldsPaul Zech , Andreas Otto , and Günter Radons*Institute of Physics, Chemnitz University of Technology, Chemnitz, Germany*

(Received 11 March 2020; accepted 8 April 2020; published 29 April 2020)

We aim at an understanding of the dynamical properties of a periodically driven damped harmonic oscillator coupled to a Random Field Ising Model (RFIM) at zero temperature, which is capable of showing complex hysteresis. The system is a combination of a continuous (harmonic oscillator) and a discrete (RFIM) subsystem, which classifies it as a hybrid system. In this paper we focus on the hybrid nature of the system and consider only independent spins in quenched random local fields, which can already lead to complex dynamics such as chaos and multistability. We study the dynamic behavior of this system by using the theory of piecewise-smooth dynamical systems and discontinuity mappings. Specifically, we present bifurcation diagrams and Lyapunov exponents as well as results for the shape and the dimensions of the attractors and the self-averaging behavior of the attractor dimensions and the magnetization. Furthermore we investigate the dynamical behavior of the system for an increasing number of spins and the transition to the thermodynamic limit, where the system behaves like a driven harmonic oscillator with an additional nonlinear smooth external force.

DOI: [10.1103/PhysRevE.101.042217](https://doi.org/10.1103/PhysRevE.101.042217)**I. INTRODUCTION**

This work is motivated by problems, which arise if a dynamical system contains a hysteretic subsystem. Hysteresis phenomena in general can be found in many different research fields, such as magnetic effects at oxide interfaces [1], shape memory alloys [2], ultrathin single-layer films [3], organic ferroelectrics [4], soft porous crystals [5], atomtronics [6], and metallic nanoparticles [7]. An overview over the field of hysteresis can be found in Ref. [8]. In general, hysteresis means that the instantaneous output depends not only on the current input value but also on its history. Thus, systems with hysteresis are systems with memory. For example, in the case of magnetic materials this means that the magnetization and the orientation of the magnetic domains depend not only on the current external magnetic field but also on its past behavior. In contrast to simple bistability, *complex* hysteresis is characterized by multistability, i.e., multiple internal states are possible for a single input value, and nonlocal memory, i.e., different internal states are connected to a given output value. As a consequence, not only one major loop but also various small subloops may appear in systems with complex hysteresis.

One of the most prominent model for complex hysteresis is the Preisach model [9]. It is a purely phenomenological model and a superposition of rectangular hysteresis loops, which are the elementary building blocks, also called Preisach units. In contrast to the Preisach model a more physical way to model hysteresis is the zero-temperature RFIM [10,11]. In the Ising model hysteresis appears because of the interaction between spins, which represent, for instance, magnetic or dielectric dipole moments of atoms. This paper serves as preparatory work for studies of the zero-temperature RFIM initially established to study phase transitions with a renormalization group approach [12]. In addition to the usual Ising model each spin in the RFIM has its own local quenched disorder field,

which in general leads to “smooth” hysteresis loops instead of “hard” jumplike loops appearing in the normal Ising model. The RFIM shows many properties, which can be also found in the Preisach model [13], but in contrast to the Preisach model, the RFIM is a spatially extended model.

Typically, the dynamical interaction of a hysteretic subsystem (hysteretic transducer) with some environment can be considered in two different ways. In the first scenario, the hysteretic transducer handles the input from the environment and produces the output of the system without feeding back to the environment. In contrast, in the second scenario the feedback of the hysteretic transducer to the environment is not negligible. In this case, a dynamical model, e. g., in form of an Ordinary Differential Equation (ODE), is necessary for describing the environmental behavior. Many results in the literature on hysteretic systems can be attributed to the first scenario [13–20]. Other studies without feedback focus on thermal relaxation processes [21,22] or the power spectral density of stochastically driven Preisach models [23–28]. On the other hand, not much is known about the second scenario, i.e., hysteretic systems coupled to their environment via a feedback mechanism. The general difficulty for such problems lies in the model for the hysteresis and the resulting dynamical systems. For example, for the Preisach model or the RFIM one obtains coupled ODE-Preisach-operator equations or piecewise smooth hybrid dynamical system, respectively. Some work has been done on ODEs coupled to a Preisach operator. The ferroresonance phenomenon in LCR circuits with an inductance modeled by a Preisach operator is studied in Refs. [29,30], and the mechanical equivalent, an iron pendulum in a magnetic field, has been studied in Ref. [31], where the hysteresis appears because of the interaction between the ferromagnetic iron mass and the magnetic field.

In a general manner, we are interested in such dynamical systems with hysteresis. As a prototypical example we consider a driven harmonic oscillator similar to Ref. [31], but in

contrast to Ref. [31], the dynamics of the magnetization of the iron pendulum is modeled by a bulk of Ising spins.

As a first step, especially in this paper, we neglect spin-spin interactions, and we will focus on systems with nearest-neighbor interactions in following papers. The absence of spin-spin interactions means that the system does not have nonlocal memory and no hysteresis between the intensity of the magnetic field and the magnetization of the pendulum is possible. However, this simplified system of a pendulum coupled to a RFIM with independent spins already shows very complex behavior. On the one hand, the dynamics of the system is quite interesting, because of the hybrid character of the system with discrete internal states of the Ising spins and a continuous nature of the pendulums motion. Such kinds of system are called piecewise-smooth hybrid systems and can be found in many fields and in every system where a sudden change of the dynamics appears. Typical examples are relay feedback systems [32–34] or mechanical systems with strong impacts, such as impact moling, ultrasonic assisted machining [35], gear dynamics including backlash [36], or systems exhibiting dry friction [37,38]. An overview of this topic can be found in Ref. [39]. On the other hand, we are indeed neglecting the memory and therefore the hysteresis in the system, but the disorder of the random fields of the Ising spins can cause some interesting issues when dealing with physical properties of the system because of the dependence on the actual disorder realization. Therefore questions of self-averaging arise.

The paper is organized as follows. In Sec. II we give a brief introduction to our model, which basically consists of two parts: an oscillator model and an Ising model. Because of the hybrid character of the system, in Sec. III we briefly introduce specific methods for piecewise-smooth systems, derive the thermodynamic limit in the case of an infinite number of spins, and make some remarks on the numerical calculation of the trajectories and the Lyapunov exponents. In Sec. IV we present characteristic results on the dynamics of the system with one spin as well as the system with many spins, the transition from the piecewise-smooth hybrid system to the smooth system in the thermodynamic limit, and the self-averaging behavior of the attractor dimensions and the magnetization. We end with a conclusion and an outlook on future work in Sec. V.

II. MODEL

Our dynamical system basically consists of two subsystems. One part is the continuous subsystem given by a periodically driven damped harmonic oscillator as described in Sec. II A. The second part is the discrete subsystem eventually given by the full RFIM and described in Sec. II B. A mechanical example for such a system, which can be realized in experiments, is illustrated in Fig. 1.

A. Oscillator model

We consider a periodically driven damped harmonic oscillator with an iron mass subject to an external magnetic field (see Fig. 1). The position of the iron mass $x(t)$ can be

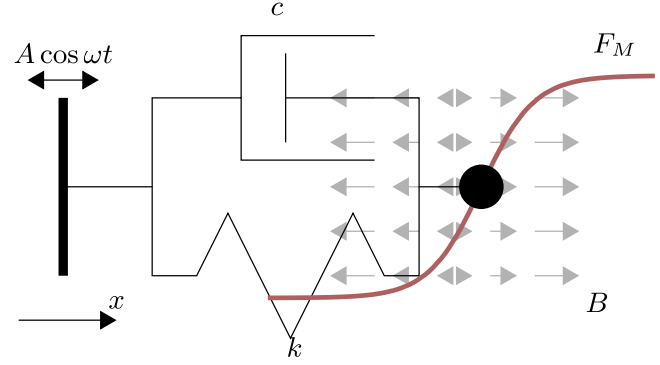


FIG. 1. Illustration of the prototypical example of a dynamical system with external force F_M (red curve), because of the interaction between the iron mass (black disk) and the external magnetic field (gray arrows). Here the external force shows non hysteric behavior because of the neglected nearest-neighbor interaction.

determined by [31]

$$m x''(\vartheta) + c x'(\vartheta) + k x(\vartheta) = A \cos \omega \vartheta + F_M(\vartheta), \quad (1)$$

where m , c , and k are the mass, damping, and stiffness of the oscillator, respectively, and A and ω are the amplitude and the angular frequency of the periodic excitation, respectively. F_M denotes the additional force, which comes from the interaction of the iron mass with the external magnetic field and is described in detail below.

The oscillator model Eq. (1) is put into a dimensionless form by using the transformations $t = \sqrt{k/m} \vartheta$ and $q(t) = \frac{k}{A} x(\vartheta)$. Thus, we obtain

$$\ddot{q}(t) + 2\zeta \dot{q}(t) + q(t) = \cos \Omega t + F(t), \quad (2)$$

where ζ denotes the damping ratio, Ω is the dimensionless excitation frequency, and $F(t) = \frac{F_M(\vartheta)}{A}$. Note that the angular eigenfrequency of the oscillator in Eq. (2) is equal to one, which means that the resonant forcing is given by $\Omega = 1$ and the period of the resonant oscillation is equal to 2π . Later we will see that the additional force will be piecewise constant $F(t) = \text{const} = CM$, which allows us to give an explicit solution for Eq. (2) with $q(t=0) = q_0$ and $\dot{q}(t=0) = v_0$ in the case of moderate damping $\zeta > 1$:

$$\begin{aligned} q(t) = & CM + \frac{1}{\kappa} [2\Omega\zeta \sin \Omega t - (\Omega^2 - 1) \cos \Omega t] \\ & + \frac{1}{2\kappa\eta} e^{-\zeta t} \{ 2\eta \cos \eta t [\Omega^2 - 1 + \kappa(q_0 - CM)] \\ & - \sin \eta t [2\zeta(\Omega^2 + 1) - 2\kappa(v_0 + q_0\zeta - \zeta CM)] \}, \end{aligned} \quad (3)$$

where a and b are given by

$$\kappa = (\Omega^2 - 1)^2 + 4\Omega^2\zeta^2, \quad (4)$$

$$\eta = \sqrt{1 - \zeta^2}. \quad (5)$$

We will use this solution later to avoid numerical integration, when simulating the system (see Sec. III D), and also to analytically calculate bifurcation points for single-spin dynamics (see Sec. IV A).

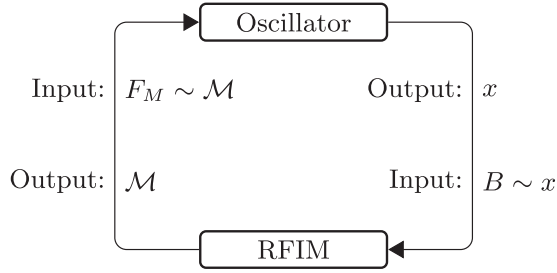


FIG. 2. The feedback mechanism of the RFIM coupled to a harmonic oscillator: The actual position x of the oscillator affects the magnetic field B (input) of the RFIM. Therefore the spin configuration and the magnetization \mathcal{M} (output) depend on x . Then the magnetization again acts on the oscillator as an additional external force.

B. Random field Ising model

For completeness and later reference we introduce here the general RFIM with nearest neighbor couplings and its zero-temperature dynamics. It simplifies considerably for independent spins as detailed in Sec. II C.

The RFIM is used to determine the magnetic force $F(t)$ that acts on the iron mass. The input and output of the RFIM is the external magnetic field B and the magnetization \mathcal{M} of the iron mass, respectively, which in general is depending on the position of the mass. (cf. Fig. 2). The total magnetization results from a superposition of the magnetization of N discrete spins, whose states are given by $\sigma_i \in \{-1, +1\}$. Consequently, the RFIM is a discrete subsystem because the total magnetization can take only a discrete set of values, which is also known as quantization (see, e.g., Ref. [40]). Moreover, the spin flips are assumed to occur instantaneously, which means that also the change of the magnetization occurs instantaneously equivalent to an impact.

The energy of a specific configuration of the RFIM can be given by its Hamilton function

$$\mathcal{H} = -\tilde{J} \sum_{\langle ij \rangle} \sigma_i \sigma_j - \mu_B \sum_i (B + \tilde{b}_i) \sigma_i, \quad (6)$$

where \tilde{J} is the coupling constant between two spins, μ_B is the magnetic moment, and \tilde{b}_i is the local field of the i th spin. The $\langle ij \rangle$ indicates a sum over nearest-neighbor pairs, where each pair of spins is only counted once. Since we are interested in a coupling of the mechanical oscillator with the RFIM, the external magnetic field $B = B(q)$ is assumed to be a function of the oscillator position q . In the following, we focus on the case of a linear dependence

$$B(q) = \beta_0 + \beta_1 q, \quad (7)$$

which means that the oscillator displacements are linearly coupled to the variations of the magnetic field. Similar to the continuous subsystem we will use a dimensionless Hamiltonian for the RFIM

$$H = \frac{\mathcal{H}}{\mu_B \beta_1} = -J \sum_{\langle ij \rangle} \sigma_i \sigma_j - \sum_i (q + b_i) \sigma_i, \quad (8)$$

where $J = \frac{\tilde{J}}{\mu_B \beta_1}$ and $b_i = \frac{\tilde{b}_i + \beta_0}{\beta_1}$ are the dimensionless coupling constant and the dimensionless local disorder field, respectively. The values $b_i, i = 1, \dots, N$ are parameters of a specific realization of the RFIM, which are chosen randomly and kept fixed during the time evolution of the system (local quenched disorder). In particular we choose the random fields to be Gaussian distributed and uncorrelated variables with $\overline{b_i b_j} = R^2 \delta_{ij}$ and $\overline{b_i} = 0$. Here \overline{X} denotes a quenched average of X , i.e., an average over all disorder realizations of the system.

In this paper we consider the RFIM at zero temperature, which means that there are no stochastic spin flips and the system dynamics is fully deterministic. The so-called single-spin-flip dynamics is used to describe the internal dynamics of the RFIM subsystem [41,42]. In this case the RFIM changes its spin configuration only if a single spin flip would lower the energy of the subsystem, i.e., the Hamiltonian function H in Eq. (8) after the spin flip is smaller than the initial value before the spin flip. The energy difference ΔH_i for a single flip of the i th spin can be given by

$$\Delta H_i = 2\sigma_i \left[J \sum_{j \in \text{nn}(i)} \sigma_j + q + b_i \right], \quad (9)$$

where $\sum_{j \in \text{nn}(i)}$ indicates the sum of j over the nearest neighbors of the i th spin. Hence, the i th spin flips if $\Delta H_i < 0$. Equation (9) can be used to define so-called *metastable states*, which are spin configurations where no single spin flip would lower the energy of the RFIM subsystem, that is, $\Delta H_i \geq 0$ for $i = 1, \dots, N$. Hence, these metastable states fulfill the so-called *metastability condition*:

$$\sigma_i = \text{sgn}(F_i), \quad (10)$$

where $F_i = J \sum_{j \in \text{nn}(i)} \sigma_j + q + b_i$ is the *local field* of the i th spin.

Now, the dynamics of the RFIM subsystem can be described as follows. The position q of the oscillator is updated according to Eq. (2) until the energy difference for any single spin flip is lower than zero ($\Delta H_i < 0$). The spin is reversed and the energy differences ΔH_i for a possible following spin flip are calculated for the new spin configuration. This is necessary because one spin flip may cause an avalanche of spin flips. If there is another spin with $\Delta H_i < 0$, this spin is also reversed, and the procedure is repeated until the system reaches the next metastable state. If the RFIM has reached the next metastable state and Eq. (10) is fulfilled for every spin, the position q of the oscillator is updated again and the spin configuration does not change until the metastable state becomes again unstable. The present update mechanism for the RFIM is known as sequential update because the next metastable state is achieved by a sequence of single spin flips. It can be shown that during avalanches other update mechanisms, for example, parallel or synchronous update, also lead to the same metastable state. Moreover, a different order of the single spin flips also would not change the next metastable state. This is due to the so-called *no passing rule* [43], which means that no spin flips more than once (either from down to up or *vice versa*) during the transition to the next metastable state [44]. It might be worth noting that the analysis of numerical algorithms for updating the internal

states of the RFIM and its connection to graph theory is an enduring field of research [45–52].

The output of the RFIM is the normalized dimensionless magnetization M defined by

$$M = \frac{1}{N} \sum_i \sigma_i. \quad (11)$$

The connection between the dimensionless magnetization M and the original magnetization \mathcal{M} of the iron mass is given by $\mathcal{M} = \rho_m M$, where ρ_m is the magnetic dipole density. The magnetic force F_M on the oscillator can be determined by $F_M = -\partial_x \mathcal{H}$, which leads to the dimensionless force

$$F(t) = CM(t), \quad C = \frac{\mu_b \beta_1 k N}{A^2}. \quad (12)$$

At each time t the oscillator position $q(t)$ determines the spin configuration of the RFIM, and therefore the magnetization $M = M(t)$. In comparison to the oscillator dynamics the update of the RFIM can be characterized as adiabatic limit because at each time t the discrete subsystem is always in a metastable state.

C. Independent spins

In this paper, we consider the case of independent spins, i.e., $J = 0$. In this case, there are no nearest-neighbor interactions and no spin avalanches. Also the phenomena of first-order phase transition in dependence of the randomness R and of the dimension of the system vanish. Since there are no nearest-neighbor interactions the spatial arrangement of the spins is irrelevant. From Eq. (10) we find that the condition for metastable states takes the simple form

$$\sigma_i(t) = \text{sgn}[q(t) + b_i], \quad \forall i = 1, \dots, N. \quad (13)$$

Equation (13) can be understood as a definition of the spin dynamics of the system. For a given position of the oscillator at time t , each spin of the RFIM points in the direction of its local field. Thus the magnetization can be calculated by

$$M[q(t)] = \frac{1}{N} \sum_i \text{sgn}[q(t) + b_i]. \quad (14)$$

For our case of independent spins Eq. (14) directly determines the magnetization $M[q(t)]$ in dependence of $q(t)$. Therefore the metastable state is always equivalent to the ground state of the RFIM with the lowest possible energy. As a result for $J = 0$ the hysteresis feature vanishes and no memory develops in our system.

Nevertheless, the case of independent spins is not trivial because there are still discrete changes of the force $F(t)$ and the hybrid character of the system does not vanish. In fact, the limitation $J = 0$ gives us the possibility to calculate exact results for the smooth system in the limit of $N \rightarrow \infty$ and to study the transition from the hybrid system for large but finite N and the smooth system with infinite N .

III. METHOD

In this section we want to explain some details of the dynamics of the hybrid system and the calculation of Lyapunov exponents for such systems. In addition, we derive

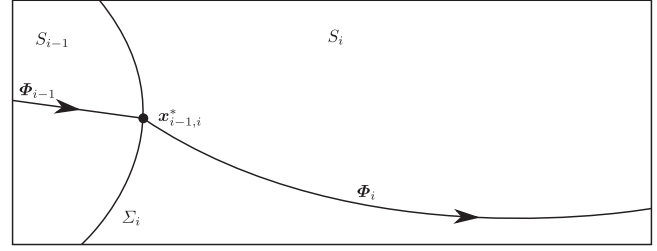


FIG. 3. An illustration of our piecewise-smooth system. The two smooth regions S_{i-1} and S_i are separated by the boundary Σ_i . The intersection point of the flow Φ_i with the boundary is called x^* .

a smooth representation in the thermodynamic limit with infinitely many spins ($N \rightarrow \infty$) and make some remarks on the implementation of the numerical methods.

A. Dynamics of the piecewise-smooth system

If the spins are ordered according to their local disorder fields b_i , it can be seen that the function $M(q)$ is a step function with $N + 1$ different levels of the magnetization at which the force F acting on the oscillator is constant

$$M_i = \frac{2i}{N} - 1, \quad i = 0, \dots, N, \quad (15)$$

implying, that $M(q)$ is piecewise constant. Such systems are called piecewise-smooth systems. The regions $\{S_i\}$ of constant F are separated by N boundaries at which the spin flips occur. Hence, one can argue that there is one ODE in each of these regions of the phase space and the system state is completely determined by knowing t , $q(t)$, and $\dot{q}(t)$. In other words, our system behaves like a piecewise-harmonic oscillator with same stiffness and same damping ratio but with a forcing which depends on the regions S_i .

Thus, we can write our system as a combination of a set of $N + 1$ ODEs:

$$\dot{\mathbf{x}}(t) = \mathbf{F}_i(\mathbf{x}(t), t) = \begin{pmatrix} v(t) \\ -2\zeta v(t) - q(t) + \cos \phi(t) + CM_i \\ \Omega \end{pmatrix}, \quad (16)$$

with $i = 0, \dots, N$. The state variable $\mathbf{x} = (q, v, \phi)^T$ is an element of the smooth regions $\mathbf{x} \in S_i$, with $\bigcup_i S_i = \mathcal{D} \subset \mathbb{R}^3$. The two-dimensional manifold $\Sigma_i = \{\mathbf{x}: H_i(\mathbf{x}) = 0\}$ with the indicator function $H_i(\mathbf{x}) = q + b_i$ separates two neighboring regions S_{i-1} and S_i . The intersection point of the trajectory with the boundaries and the flow in the region S_i is denoted by $\mathbf{x}_{i-1,i}^*$ and $\Phi_i(\mathbf{x}(t_0), t)$, respectively (see Fig. 3). An exemplary trajectory of the system with $N = 3$ spins in the state space is illustrated in a projection in Fig. 4. We consider a point on the trajectory with $q < -b_1$ [black bullet (\bullet) in left figure]. This means that all spins are in the down state. The system is evolved with magnetization $M_0 = -1$. After some time we have $-b_1 < q < -b_2$, and the first spin has been flipped to the up state. In this region of the phase space the system further evolves with magnetization $M_1 = -\frac{1}{3}$. After passing the next boundary with $-b_2 < q < -b_3$ the next spin will flip, and the magnetization is $M_2 = \frac{1}{3}$. For $q > -b_3$ all spins are in the

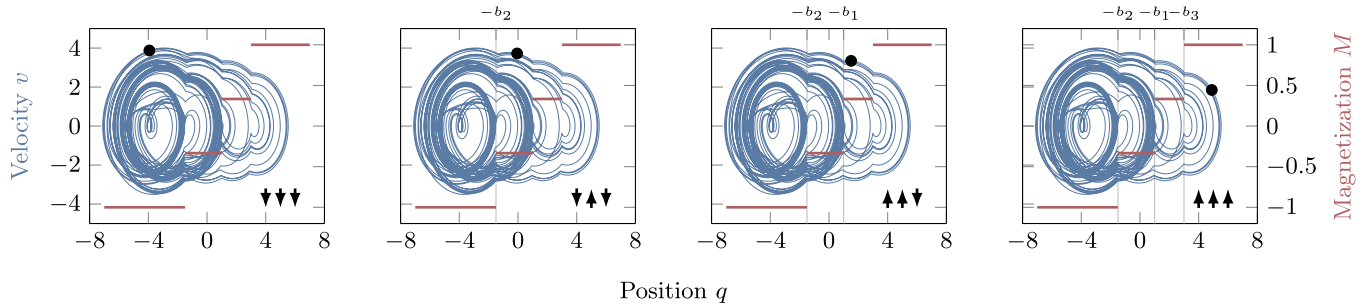


FIG. 4. Example of a projection of a state space trajectory of the harmonic oscillator coupled to $N = 3$ spins. There are four smooth regions S_i with piecewise constant magnetization (—) corresponding to four different spin configurations ($\uparrow\downarrow\uparrow$). At each of the three boundaries a jump discontinuity appears in the acceleration \ddot{q} . The values of the local disorder are $b_1 = -1.0$, $b_2 = 1.5$, and $b_3 = -3.0$.

up-state with $M_2 = 1$ (right figure). When the oscillator moves in the other direction, the spins flips occur in reverse order.

B. Thermodynamic limit $N \rightarrow \infty$

For N spins there are N boundaries, and at each boundary the magnetization increases by the value $\frac{2}{N}$. For increasing N , on one hand, the number of boundaries increases and, on the other hand, the changes of the magnetization decrease. Thus, in the limit $N \rightarrow \infty$ (thermodynamic limit) the hybrid character of the piecewise smooth system should vanish. In the following we derive a smooth function $M(q)$ for the magnetization in dependence on the oscillator position q , representing the behavior of the system in the thermodynamic limit.

For $q \rightarrow -\infty$ each spin is in the down state and the magnetization is given by $M = -1$. For increasing q the magnetization increases monotonically and in the limit $q \rightarrow +\infty$ we have $M = +1$. The specific shape of the function $M(q)$ is determined by the positions of the boundaries. Since the location of the boundaries is determined by the local disorder b_i , the probability density of the boundaries is a Gaussian distribution $p(q)$ with zero mean and standard deviation R . The associated cumulative distribution can be written as

$$P(q) = \int_{-\infty}^q p(q') dq' = \frac{1}{2} \left[1 + \operatorname{erf} \left(\frac{q}{R\sqrt{2}} \right) \right]. \quad (17)$$

It determines the ratio between the number of spins in the down state and the number of all spins in dependence of the oscillator position q . Therefore, in the limit $N \rightarrow \infty$ we can substitute the ratio $\frac{i}{N}$ in Eq. (14) by $P(q)$ and obtain a smooth function for the magnetization

$$M[q(t)] = 2P[q(t)] - 1 = \operatorname{erf} \left[\frac{q(t)}{\sqrt{2}R} \right]. \quad (18)$$

This means that in the limit $N \rightarrow \infty$ our smooth dynamical system consisting of a driven damped harmonic oscillator coupled to a RFIM with infinitely many independent spins can be described by

$$\dot{\mathbf{x}}(t) = \begin{pmatrix} v(t) \\ -2\zeta v(t) - q(t) + \cos \phi(t) + C \operatorname{erf} \left[\frac{q(t)}{R\sqrt{2}} \right] \\ \Omega \end{pmatrix}, \quad (19)$$

with a smooth nonlinearity given by the error function. Thus, in Eq. (19) the feedback from the RFIM is characterized by an additional nonlinear external force that depends on the oscillator position $q(t)$. In Sec. IV we compare the dynamics of the piecewise smooth system Eq. (16) with a large but finite number of spins N and the dynamics of the smooth system Eq. (19) with infinitely many spins.

C. Lyapunov exponents

Lyapunov exponents are defined as the average rate of divergence or convergence between a reference trajectory and a perturbed trajectory, where the perturbations are infinitely small. For the smooth dynamical system Eq. (19) we use the standard method [53] for calculating Lyapunov exponents. We use the same method in the smooth regions S_i of the piecewise smooth system Eq. (16). However, if the reference trajectory crosses a discontinuity boundary, the determination of the dynamic behavior of the infinitesimal perturbations is not straightforward because the perturbed trajectory may have crossed or may cross the boundary at an earlier or a later time instant, respectively. In general, in the neighborhood of the discontinuities a careful treatment of the determination of the perturbations is necessary because the switching behavior of the perturbed trajectory is typically different from the switching behavior of the reference solution. The compensation of such deviations can be done by using the concept of the so-called Discontinuity Map (DM) [54–57]. In the following, we describe at first the basic concept of the DM for transversal intersections of the boundary, where the reference trajectory crosses the boundary. Later we recall the concept of gracing intersections, where the reference trajectory hits the boundary tangentially.

1. Transversal intersection: Discontinuity mapping

During the calculation of the Lyapunov exponents we know only the time instant t^* , where the reference trajectory reaches a discontinuity boundary and where we switch between two different ODEs. At t^* the perturbed state is in the neighborhood of the boundary but may have crossed it in the past or will cross it in the future. If the perturbed trajectory crossed (will cross) the boundary at an earlier (a later) time $t^* + \delta t$ with $\delta t < 0$ ($\delta t > 0$), the DM predicts the crossing time $t^* + \delta t$ by using knowledge of the state \mathbf{x}^* , approximates the perturbed state at the crossing time, applies

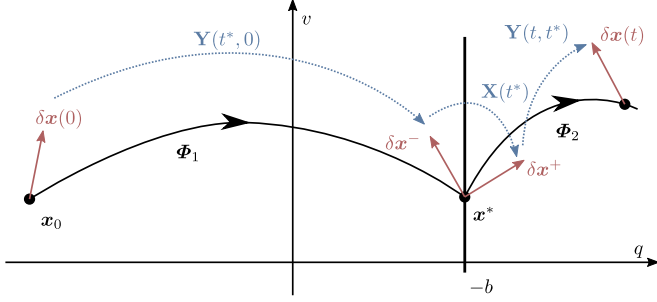


FIG. 5. Illustration of the calculation of the Lyapunov exponent for piecewise-smooth systems. To evolve a small perturbation δx in the smooth region, we can use the fundamental solution $\mathbf{Y}(t_2, t_1)$ of the variational equation of the ODE. The effect of the boundaries on δx is described by the saltation matrix \mathbf{X} .

the effects from the discontinuity crossing, and approximates the perturbed state at time t^* by evolving the perturbations before intersecting the boundary to the perturbations after the dynamics has been switched. In other words, the DM immediately incorporates the effects of a discontinuity crossing even if the state is only in the neighborhood of a boundary and the crossing appeared in the past or will appear in the future. For our system, the DM from a region S_i to a region S_j can be given by the map \mathcal{Q}_{ij} :

$$\mathbf{x} \rightarrow \mathcal{Q}_{ij}(\mathbf{x}) = \begin{pmatrix} q \\ C(M_i - M_j)\delta t + v \\ \phi \end{pmatrix}, \quad (20)$$

where $\delta t = \frac{q^* - q}{v^*}$. Since there is only a force jump at the boundary the DM changes only the velocity of the state variable. Note that only changes with $|i - j| = 1$ are possible and that the change in the magnetization is $\Delta M = M_j - M_i = \pm 2$.

For infinitely small perturbations δx the Jacobian $\mathbf{X} = \partial_x \mathcal{Q}(\mathbf{x})$ of the DM evaluated at the intersection point \mathbf{x}^* can be used to calculate the perturbation $\delta x^+(t^*)$ after the crossing by

$$\delta \mathbf{x}^+(t^*) = \mathbf{X} \delta \mathbf{x}^-(t^*), \quad (21)$$

where $\delta \mathbf{x}^-(t^*)$ denotes the perturbation before the intersection with the boundary. The matrix \mathbf{X} is called *saltation matrix*. For our system it has the form

$$\mathbf{X} = \begin{pmatrix} 1 & 0 & 0 \\ \frac{1}{v^*} C \Delta M & 1 & 0 \\ 0 & 0 & 1 \end{pmatrix}. \quad (22)$$

Then, for a trajectory with only one crossing at time t^* the largest Lyapunov exponent would be defined as

$$\lambda = \lim_{t \rightarrow \infty} \frac{1}{t} \ln \frac{|\mathbf{Y}(t, t^*) \mathbf{X} \mathbf{Y}(t^*, 0) \delta \mathbf{x}_0|}{|\delta \mathbf{x}_0|}, \quad (23)$$

where $\mathbf{Y}(t, t')$ is the fundamental solution of the variational equation $\delta \dot{\mathbf{x}}(t) = \mathbf{D} \delta \mathbf{x}(t)$ of the ODE (16) from time t' to t and \mathbf{D} denotes the Jacobian. The calculation of the Lyapunov exponent via Eq. (23) is illustrated in Fig. 5 and can be explained as follows. We start with an initial perturbation

$\delta \mathbf{x}_0$ at time $t = 0$, and evolve the perturbations up to the intersection time t^* , which is calculated from the reference trajectory. At this point we have $\delta \mathbf{x}^-(t^*) = \mathbf{Y}(t^*, 0) \delta \mathbf{x}_0$. Then the effect of the DM is captured by applying the saltation matrix \mathbf{X} to $\delta \mathbf{x}^-(t^*)$. After the intersection we can use $\mathbf{Y}(t, t^*)$ again, to compute the perturbation up to time t . Note that the Jacobian \mathbf{D} and consequently the fundamental solution $\mathbf{Y}(t, t')$ is independent of the associated phase space region S_i because only a constant term, i.e., the magnetization M_i , changes at the boundaries in the ODE (16).

2. Grazing intersection: Poincaré section and zero-time discontinuity mapping

Note that the saltation matrix has a singularity for $v_* \rightarrow 0$, when the trajectory hits the boundary tangential. This case is called the *grazing intersection*. In general grazing occurs if the trajectory hits the boundary tangentially with the velocity normal to the boundary being equal to zero. The point \mathbf{x}^* , which belongs to the grazing intersection, is called the *grazing point*. Similar to the case of transversal intersections, we have to make a correction, when calculating Poincaré maps for trajectories starting near a orbit, which grazes the boundary. These correction arise because some trajectories will not intersect the boundary, whereas others do cross. There are two common corrections to this, called Poincaré Section Discontinuity Mapping (PDM) \mathcal{Q}^P and Zero Time Discontinuity Mapping (ZDM) \mathcal{Q}^Z [58]. Both corrections are constructed in the same manner as the transversal DM, and they are describing the same grazing scenario. But whereas the PDM is defined with respect to a given Poincaré section, the ZDM is defined such that zero time has been elapsed between perturbation before and after the intersection with the boundary.

It has been shown that in the case of the degree of smoothness of one, one has to add square-root terms of \mathbf{x} in the mapping of points near grazing [57]. For the artificial example illustrated in Fig. 5 the grazing point is given by $\mathbf{x}^* = (-b, 0, \phi^*)^T$, hence the PDM takes the following form:

$$\mathbf{x} \rightarrow \mathcal{Q}^P(\mathbf{x}) = \begin{cases} \mathbf{x} & \text{for } H = q + b < 0, \\ v_z \sqrt{q + b} & \text{for } H = q + b > 0, \end{cases} \quad (24)$$

$$v_z = 2\sqrt{2} \frac{C\Omega(M_1 - M_2)}{(b + \cos \phi^* + CM_2)(b + \cos \phi^* + CM_1)^{\frac{1}{2}}} \begin{pmatrix} 0 \\ 0 \\ 1 \end{pmatrix}, \quad (25)$$

and the corresponding ZDM can be written as

$$\mathbf{x} \rightarrow \mathcal{Q}^Z(\mathbf{x}) = \begin{cases} \mathbf{x} & \text{for } H_{\min} < 0, \\ v \sqrt{H_{\min}} & \text{for } H_{\min} > 0, \end{cases} \quad (26)$$

$$v = 2\sqrt{2} \frac{C(M_2 - M_1)(b + \cos \phi^* + CM_1)}{(b + \cos \phi^* + CM_2)(b + \cos \phi^* + CM_1)^{\frac{1}{2}}} \begin{pmatrix} 0 \\ 1 \\ 0 \end{pmatrix}, \quad (27)$$

where $H_{\min}(\mathbf{x})$ is the minimum value of $H(\mathbf{x})$ obtained along the flow $\Phi_1(\mathbf{x}, t)$, where \mathbf{x} is an arbitrary point near the grazing point \mathbf{x}^* .

For piecewise-smooth systems with a degree of smoothness of one it has been shown that the dynamics—especially

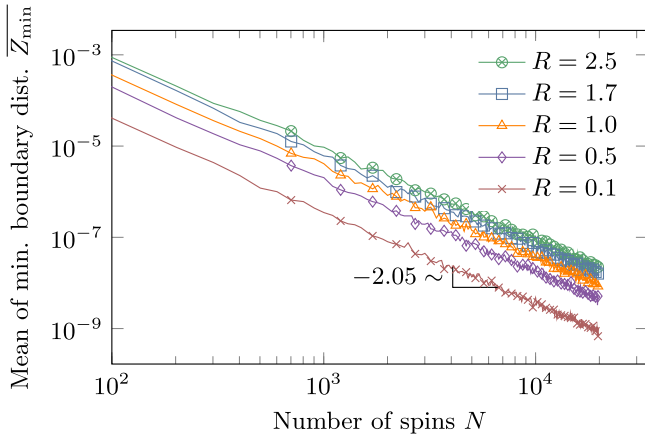


FIG. 6. Dependency of the mean of the minimal value of the distances between two boundaries $\overline{Z_{\min}}$ on the number of spins for different values of randomness R . The mean $\overline{Z_{\min}}$ was calculated for 500 different realizations of b_i .

the different scenarios, which can occur in bifurcation diagrams—can be explained by piecewise-smooth discontinuous square-root maps like (25) [58]. The analysis of piecewise-smooth square-root maps reveals that those maps can describe various bifurcation scenarios including period adding and robust chaos [59–61].

D. Numerics

In general for $J \neq 0$ the generation of trajectories of the hybrid system is done in the following way. The external force of the initial metastable state of the RFIM is determined and used to solve the continuous subsystem until the next boundary is reached, i. e., until the metastable state of the RFIM becomes unstable. Then the new metastable state of the RFIM is calculated by using the single-spin-flip update, and the external force corresponding to the new metastable state of the RFIM is used to solve the continuous subsystem up to the next boundary crossing.

In our case of $J = 0$ the simulation of the RFIM becomes obsolete, because of the absence of memory in the system. Hence, from the indicator function $H_i(x) = 0 = q + b_i$, we can determine the boundaries in the phase space directly before starting the actual propagation of the trajectories (see Sec. III A). Also, since the continuous subsystem is linear between the boundaries, it is possible to analytically calculate the trajectory of the oscillator for a fixed external magnetic force [see Eq. (3)]. Nevertheless we are not able to calculate the time the oscillator needs propagating from one boundary to the next. In doing so we would have to solve Eq. (3) for t , and this can not be done in a analytic way. Therefore for a low number of spins, i.e., a “large” distance between two boundaries, we then use the analytical solution with a fixed step size Δt to propagate the trajectory until a boundary given by $0 = q + b_i$ is crossed. Then a root finder is used to calculate the exact time t^* and state \mathbf{x}^* at the intersection point. The step size Δt is chosen according to the results in Fig. 6 such that no boundary crossings will be skipped.

For an increasing number of spins in the system, the number of boundaries becomes large and the distances between

two boundaries decrease. Thus if the number of spins is large, we use an adaptive scheme to solve the system, because the performance of the above-mentioned numerical solution with a root finder is low for large N . However, in this case, there are still regions in the phase space where the distance between two boundaries is large. This holds, for example, at very low and high values of q , where the probability for the occurrence of a boundary is small. In these regions, we again use the analytical solution of the continuous subsystem in combination with the root finder. On the other hand, if the distance between two boundaries becomes “small,” we calculate the next intersection point (t^*, \mathbf{x}^*) directly by assuming a constant velocity of the oscillator between two boundary crossings. This is similar to a linearization of Eq. (3). By using this adaptive method, we are able to generate bifurcation diagrams with a finite but very high number of discontinuities (see Sec. IV).

To get quantitative information on the size of “small” and “large” distances between two boundaries and how to choose the corresponding step size Δt , such that no boundary crossings will be skipped, we calculated the expectation value for the minimum distance between two boundaries from the probability distribution of the local disorder values b_i in dependence on the number of spins and the randomness R . Specifically, the local disorder values b_i can be written as a multivariate random variable $\mathbf{b} = (b_1, b_2, \dots, b_N)$, where the b_i are independent and identically distributed random variables with $b_i \sim \mathcal{N}(0, R^2)$. Since we are interested in the distances between two boundaries, we consider one sorted realization of \mathbf{b} , called $\mathbf{s} = (s_1, s_2, \dots, s_N)$ with $s_1 \leq s_2 \leq \dots \leq s_N$. Hence, we can define the distance between consecutive boundaries for one realization as $\mathbf{z} = (z_1, z_2, \dots, z_{N-1})$ and $z_i = s_{i+1} - s_i$, and denote z_{\min} the minimum of \mathbf{z} . Because z_{\min} depends on the realization of \mathbf{b} , there is a related random variable Z_{\min} . The dependence of the expectation value $\overline{Z_{\min}}$ on the number of spins N for different values of R is presented in Fig. 6, where \overline{X} indicates the expectation value for the random variable X over different realizations of \mathbf{b} . It can be seen, that for an increasing number of spins, the mean minimal distance decreases algebraically to zero with an exponent of roughly $N^{-2.05}$.

IV. RESULTS

In this section we present the main results, starting with the single-spin and many-spin dynamics. Next we study the transition to the thermodynamic limit, i.e., the transition from the piecewise-smooth system with an increasing number of spin-flip boundaries to the smooth system. Moreover, we present some results on the fractal dimensions of the chaotic attractors and take a look at the behavior of the magnetization for an increasing number of spins. All numerical simulations have been done by fixing the normalized eigenfrequency as $\Omega = 1.0$ and the damping ratio of the harmonic oscillator as $\zeta = 0.05$.

A. Single-spin dynamics

We start by investigating the dynamic behavior of the system with one spin $N = 1$. We have calculated the largest Lyapunov exponent and bifurcation diagrams for different

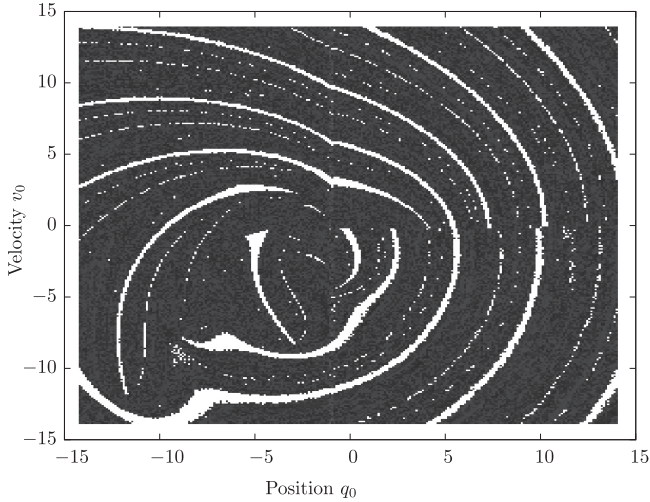


FIG. 7. The system with one boundary at $x = -0.6$ shows a sensitive dependence of the asymptotic solution on the initial conditions. Black boxes (■) indicate chaos with a largest Lyapunov exponent greater than zero, while the white boxes (□) correspond to periodic behavior. The parameters are $b_1 = 0.6$ and $C = 1.65$ in Eqs. (13) and (16) for $N = 1$.

initial values q_0 and v_0 . We have found multistability in a various parameter ranges. According to Eqs. (13) and (16) with $N = 1$, an exemplary basin of attraction for the parameters $b_1 = 0.6$ and $C = 1.65$ is presented in Fig. 7, where chaotic solutions with a largest Lyapunov exponent greater than zero and periodic solutions with vanishing Lyapunov exponent are indicated by black and white boxes, respectively. One can see the effects from the discontinuity at the position of the spin flip $q = -b_1 = -0.6$ and at $v = 0$, where the saltation matrix has a singularity. Multistability can be observed for the asymmetric case with $b_1 \neq 0$. In contrast, for $b_1 = 0$ the spin flip position would be equivalent to the equilibrium position of the oscillator, and in this case no multistable behavior can be observed.

A typical bifurcation diagram for the symmetric case ($b_1 = 0$) is presented in Fig. 8. It shows the displacement of the oscillator $q(\phi = 0)$ at the Poincaré section $\phi = 0$ and the corresponding Lyapunov exponent of the asymptotic solution. The bifurcation diagram is generated with the fixed initial conditions $q_0 = -1.0$, $v_0 = 0.1$ by varying the coupling parameter C . The system shows the typical scenarios, which are known for piecewise-smooth square-root maps [59–61]. This is in accordance with the actual square-root dependence of the PDM and ZDM from Eq. (25) and Eq. (27) found for our system. The three corresponding bifurcation scenarios, which appear due to the discontinuity with degree of smoothness one, are outlined by the three colored boxes in Fig. 8. The green box demonstrates an overlapping period-adding cascade, which in the case of decreasing values of C starts at $C^* = 10$. This is in agreement with the prediction we can make by using the solution of the harmonic oscillator with constant magnetization from Eq. (3). When starting at the left side of the boundary $q^* = 0$ we can calculate for large t the maximum q values of the periodic orbit of the system. By assuming that this orbit touches the boundary if $q_{\max} = q^*$,

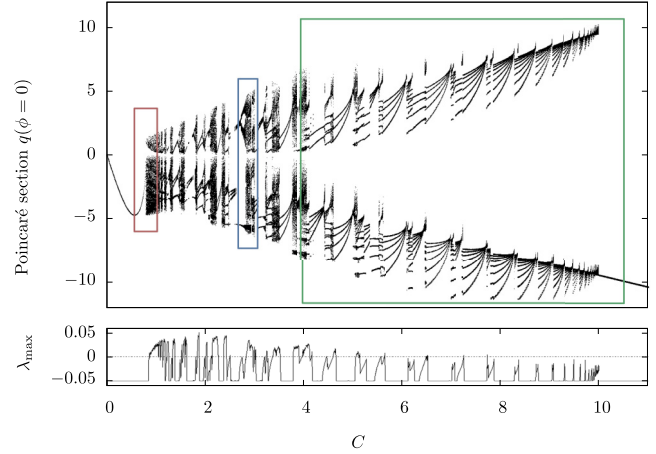


FIG. 8. Bifurcation diagram for the totally symmetric system with $N = 1$ and $b_1 = 0$. The system shows the bifurcation scenarios expected from piecewise-smooth square-root maps, illustrated by the different colored boxes (from left to right): immediate jump to robust chaos (—), period-adding with chaos (—), and overlapping period-adding cascade (—).

we find a formula for C^* :

$$C^* = \frac{1}{M} \left(q^* - \frac{1}{\sqrt{\kappa}} \right). \quad (28)$$

For $M = -1$, $q^* = 0$, and $\zeta = 0.05$ we find $C^* = 10$. The blue box illustrates period adding with chaotic segments in between, and the red box shows an immediate jump from chaos again to a periodic solution. For a nonzero disorder parameter $b_1 \neq 0$, in general, the qualitative behavior of the bifurcations is similar to the bifurcations in the symmetric case. However, in the asymmetric case $b_1 \neq 0$ the location of the periodic windows and the chaotic regions can slightly change depending on the specific initial condition. Moreover, it is worth emphasizing that the system without discontinuity ($N = 0$) does not show any chaos because it reduces to the dynamics of a damped harmonic oscillator with periodic excitation. This means that the origin of chaos in the system with one spin is the piecewise constant magnetization that jumps at the spin flip position.

B. Many-spin dynamics

For systems with a few number of spins the dynamic behavior and the bifurcation diagrams look similar to the one spin case, and only the number of discontinuities may be different. However, if the number of spins is much higher than one, the characteristic properties of the system change. A bifurcation diagram and the corresponding Lyapunov exponent for a high number of spins $N = 20\,000$ and a fixed realization of b_i is presented in Fig. 9. In this case and for all following numerical calculations the degree of randomness of the disorder is chosen as $R = 1.7$. First, we report that the largest Lyapunov exponent λ_{\max} for the many-spin system evaluated for chaotic regions is roughly two times larger than λ_{\max} of the system with only one spin. This is not obvious, because for an increasing number of spins the height of the magnetization jumps at the boundaries goes to zero and the

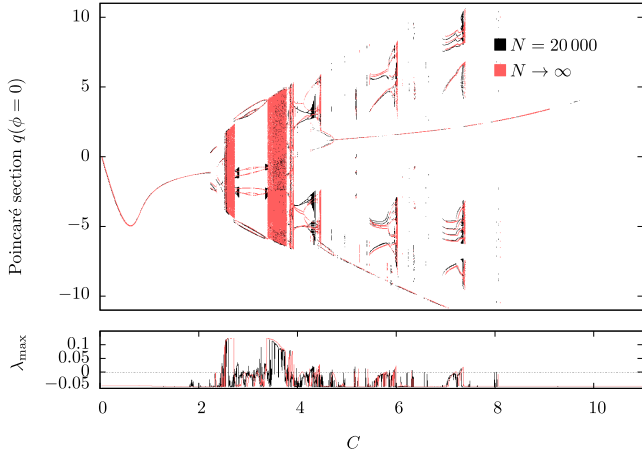


FIG. 9. Comparison of the bifurcation diagrams for the piecewise-smooth system with $N = 20\,000$ (■) spins and the system in its thermodynamic limit (■). It can be seen that the typical grazing scenarios (immediate jump to chaos and period-adding cascades) vanish, whereas the main behavior is pretty similar.

saltation matrix converges to the identity. On the other hand, the typical bifurcation scenarios from grazing (period adding, immediate jump to chaos) vanish, which is also not obvious because the number of boundaries and discontinuities is much higher than for the one-spin system. This indicates that the chaotic behavior arises only due to transversal intersections with the boundaries. The dynamic properties of the system with many spins are, in general, very similar to the dynamic properties of the smooth system in the thermodynamic limit ($N \rightarrow \infty$). This can be seen, for example, by comparing the bifurcation diagram and the maximum Lyapunov exponent of the piecewise-smooth system with $N = 20\,000$ spins and their counterparts calculated from the smooth system, which are presented by the red curves in Fig. 9. Overall both the black curves for the piecewise-smooth system and the red curves for the continuous system look very similar. But a more detailed view (see Fig. 10) of the bifurcations for $C \in [2, 3]$ shows that the two diagrams are slightly different. This is due to the fact that even for $N = 20\,000$ the behavior of the system depends to be noticeable on the actual realization of the disorder $\{b_i\}$. The same observation can be made in the comparison of the chaotic attractors of the smooth and the piecewise-smooth system, which are presented in Fig. 11. There are nearly no differences in the macroscopic structure of the attractor, and only small deviations can be seen at finer scales.

C. Transition to the thermodynamic limit

In the piecewise-smooth system with a finite number of spins the origin of chaos lies in the discontinuity crossings, whereas in the smooth system with an infinite number of spins chaos comes from the nonlinearity in the additional magnetic force. Nevertheless, for an increasing number of spins the dynamics of the piecewise-smooth system converges on macroscopic scales to the dynamics of the system in the thermodynamic limit. In the following this transition is studied in more detail.

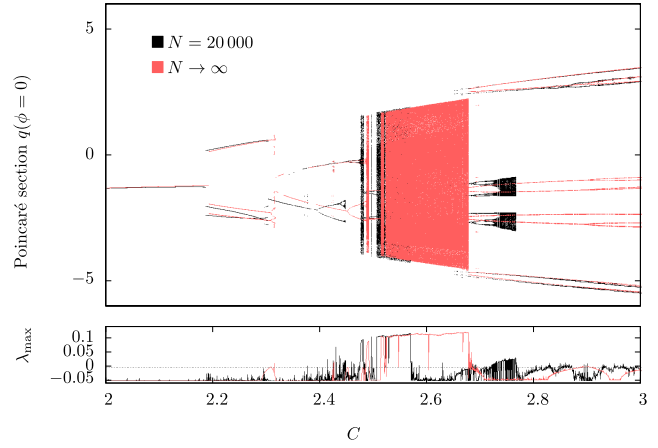


FIG. 10. Zoom of the bifurcation diagram from Fig. 9. It can be seen that besides the general similarities between the piecewise-smooth system and the system in its thermodynamic limit there are some differences in the actual behavior of the bifurcations. Mainly this is because of the dependence of the dynamical properties of the system for $N = 20\,000$ on the actual realization of the local disorder $\{b_i\}$.

On the one hand, for increasing N the number of discontinuities increases, but on the other hand simultaneously the influence of the discontinuities goes to zero, because the jump in the magnetization ΔM at each discontinuity vanishes ($\Delta M \rightarrow 0$) and the saltation matrix \mathbf{X} converges to the identity ($\mathbf{X} \rightarrow \mathbf{I}$) for $N \rightarrow \infty$. To get an idea of the interplay between the increasing number of boundaries and the decreasing influence of an individual spin flip, we consider a small segment of the attractor with length q_g , which is divided by n boundaries. For a very large number of spins, we can assume that the location of the boundaries is homogeneously distributed in the small segment with length q_g , which means that the distance between two boundaries can be approximately given by $\Delta q = q_g/n$. Note that for Gaussian-distributed local disorder fields of the RFIM the average distance Δx still varies with the location of the attractor segment in phase space. In addition, we assume the velocity at the intersection to be $0 < v < \infty$ for $\Delta M > 0$, which is a valid assumption, because a positive velocity leads to an increasing q and a positive ΔM . The short-time Lyapunov exponents can be determined by

$$\lambda_i = \frac{1}{\Delta t} \ln |\mu_i(\mathbf{XY})|, \tag{29}$$

where $\Delta t = \Delta q/v$, $\mu_i(\mathbf{A})$ denotes eigenvalues of a matrix \mathbf{A} , and the matrices \mathbf{X} and \mathbf{Y} are the saltation matrix and the fundamental solution of the harmonic oscillator for a time step Δt , respectively. They are given by

$$\mathbf{X} = \begin{pmatrix} 1 & 0 \\ \frac{1}{v}C\Delta M & 1 \end{pmatrix}, \quad \mathbf{Y} = \exp \left[\begin{pmatrix} 0 & 1 \\ -1 & -2\zeta \end{pmatrix} \Delta t \right]. \tag{30}$$

For very large N , Δt is very small and the matrix exponential in \mathbf{Y} can be approximated via a linear Taylor approximation. In this case, the Lyapunov exponents can be determined by

$$\lambda_{1/2} = \text{Re} \left[-\zeta \pm \sqrt{C \frac{\Delta M}{\Delta q} + \zeta^2 - 1} \right]. \tag{31}$$

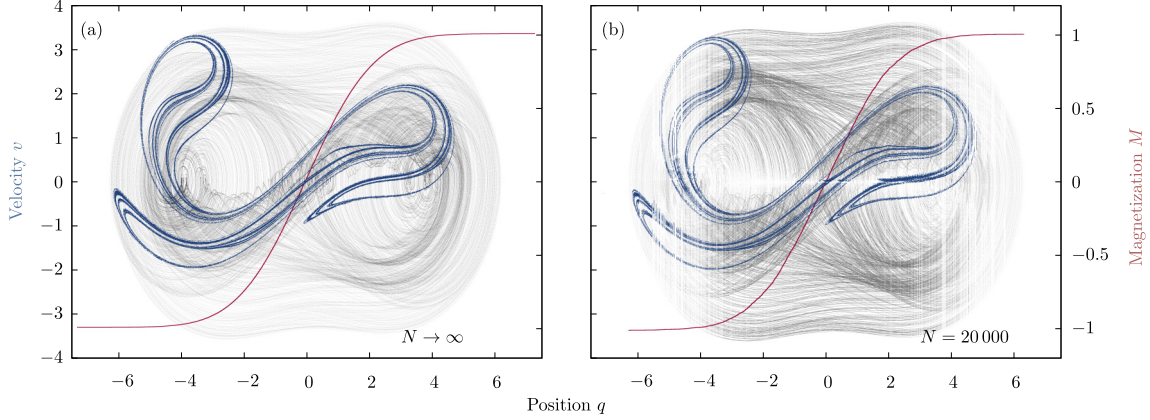


FIG. 11. Comparison of the chaotic attractor (—), Poincaré section (—), and magnetization (—). (a): The system in its thermodynamic limit $N \rightarrow \infty$. (b): The piecewise-smooth system with $N = 20\,000$ spins and one specific disorder realization $\{b_i\}$. Both systems are evaluated for fixed coupling constant $C = 3.5$ and with the randomness set to $R = 1.7$.

For $\frac{1}{C} < \frac{\Delta M}{\Delta q}$ the short-time Lyapunov exponent is positive, which means that, in general, chaotic behavior is possible. Note that for an increasing number of spins the jump of the magnetization $\Delta M = 2/N$ vanishes but simultaneously the average distance Δx between two jumps vanishes. The ratio $\frac{\Delta M}{\Delta q}$ converges to a positive constant specifying the average density of discontinuities in the given attractor segment. A high number of jumps and/or a high coupling constant C increases the short-time Lyapunov exponent and, therefore, the probability to observe chaos.

For the smooth system in its thermodynamic limit $N \rightarrow \infty$ we can find a similar condition by linearizing the nonlinear system Eq. (19) around a location q^* on the attractor. In this case, the corresponding short-time Lyapunov exponents at q^* can be calculated from Eq. (29) by substituting the matrix product \mathbf{XY} with the matrix

$$\mathbf{Y}_\infty = \exp \left[\begin{pmatrix} 0 & 1 \\ -1 + C \frac{\partial M(q)}{\partial q} \Big|_{q^*} & -2\zeta \end{pmatrix} \Delta t \right], \quad (32)$$

leading to the two Lyapunov exponents

$$\lambda_{1/2} = \text{Re} \left[-\zeta \pm \sqrt{C \frac{\partial M(q)}{\partial q} \Big|_{q^*} + \zeta^2 - 1} \right]. \quad (33)$$

By comparing Eq. (31) and Eq. (33) it becomes clear that the discrete magnetization jumps in one attractor segment of the piecewise-smooth system translate into a continuous increase of the magnetization in the smooth system, and the short-time Lyapunov exponent depends on the slope of the magnetization in this segment. By inserting the explicit expression for the derivative of the magnetization derived from the distribution of the local disorder of the spins, we obtain the condition

$$\frac{1}{C} < \sqrt{\frac{2}{\pi R^2}} e^{-\frac{q^{*2}}{2R^2}} \quad (34)$$

for a positive short-time Lyapunov exponent at q^* .

The behavior of the condition in Eq. (34) is illustrated in Fig. 12. For $C = 0$, there are two Lyapunov exponents $\lambda_{1/2} = -\zeta$ and no chaos is possible. For increasing C at

some point the term under the square root in Eq. (33) becomes positive and by further increasing C the dominant exponent becomes positive. Thus, increasing C increases the probability for observing chaos, which is clear because a higher coupling constant C leads to a higher weighting of the nonlinear magnetic force. At $q^* = 0$, corresponding to the position with the maximal density of boundaries, the dominant short-time Lyapunov exponent has its maximum, and the exponent decreases for an increasing $|q^*|$. This is clear because the maximum slope of the nonlinearity in Eq. (19), and therefore the largest influence of the magnetic force, can be found at $q^* = 0$, whereas for $q^* \rightarrow \pm\infty$ the slope goes to zero and the dependence of the magnetization on the oscillator position vanishes. The dependence of the short-time Lyapunov exponent on the variance R^2 of the local disorder can be explained as follows. For a small R^2 (large $1/R^2$ in Fig. 12) most of the spin flips occur around $q^* = 0$. There is a large change of the magnetization around the equilibrium position but only slight changes at other points, where the density for spin flips is much lower. As a consequence the short-time Lyapunov exponent is likely to be positive near $q^* = 0$ and becomes smaller and negative for increasing $|q^*|$.

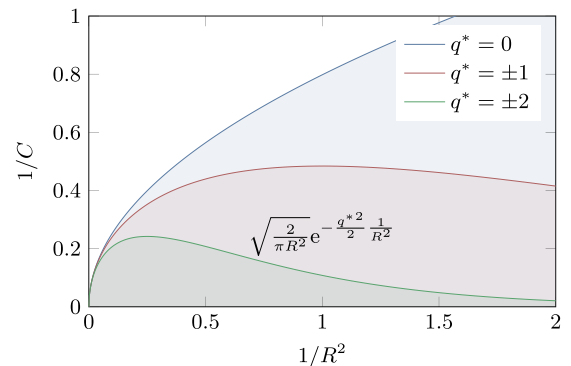


FIG. 12. Phase diagram for the short time chaotic behavior of the nonlinear system in its thermodynamic limit. The shaded areas illustrate the region with a positive short-time Lyapunov exponent at q^* .

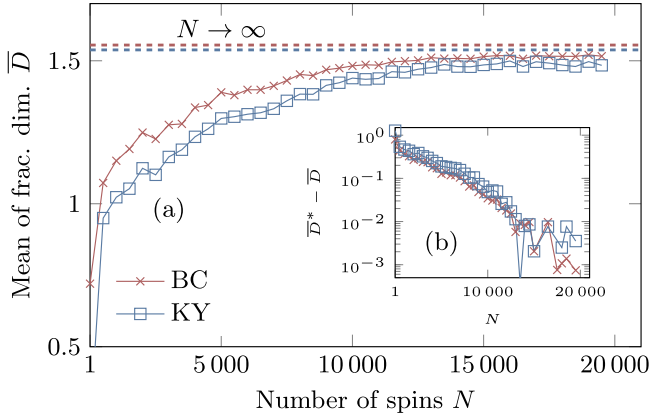


FIG. 13. (a) For an increasing number of spins the box counting (red crosses) and the Kaplan-Yorke dimension (blue squares) converge to the corresponding values of the smooth system (dashed lines) in the thermodynamic limit ($N \rightarrow \infty$). Here the coupling strength equals $C = 3.5$ in Eqs. (16) and (19). (b) There is a linear dependence of the difference between the mean of the fractal dimension and the corresponding limit value for increasing N , which can be seen in a semi-log plot. Hence there is an exponential convergence to the limit values.

In contrast, for a large variance R^2 the changes of the density for observing spin flips is low, and similarly the variations of the magnetization for varying oscillator position are low. As a consequence, a positive short-time Lyapunov exponent and probably chaos can be found only for very high C but then in a broad region around q^* .

D. Fractal dimensions of the chaotic attractor

Since the system can still produce chaos, even for an infinite number of boundaries, it is natural to ask for the dynamic properties of a typical chaotic attractor, which is shown, for example, in Fig. 11. Hence we are interested in the behavior of the box counting and the Kaplan-Yorke dimension D_{BC} and D_{KY} [62,63]. Thus we calculated the mean values of both dimensions \bar{D}_{BC} and \bar{D}_{KY} of the attractor for a varying number of spins N by using 500 different realizations of the local disorder $\{b_i\}$ at each value of N . The results are shown in Fig. 13, where the coupling strength of the magnetization is chosen as $C = 3.5$. One sees, that the mean value of the box counting and the Kaplan-Yorke dimension converges to the corresponding values of the smooth system in its thermodynamic limit. The values of both dimensions for the smooth system in its thermodynamic limit are given by $D_{BC}^\infty \approx 1.56$ and $D_{KY}^\infty \approx 1.54$ (dashed lines in Fig. 13). The limit values of the mean of both dimensions for the piecewise-smooth system are $\bar{D}_{BC}^* \approx 1.52$ and $\bar{D}_{KY}^* \approx 1.49$, calculated by using the mean of the last five fractal dimensions values from $N = 17\,500$ to $N = 19\,500$. We also plotted $\bar{D}^* - \bar{D}$ in dependence on N , which is shown in the inset in Fig. 13. We find, that \bar{D}_{BC} as well as \bar{D}_{KY} converges exponentially to their limit values \bar{D}_{BC}^* and \bar{D}_{KY}^* . This supports the proposition, that the piecewise-smooth system with a very large number of spins behaves like a harmonic oscillator with an additional nonlinear smooth external force and the piecewise-smooth

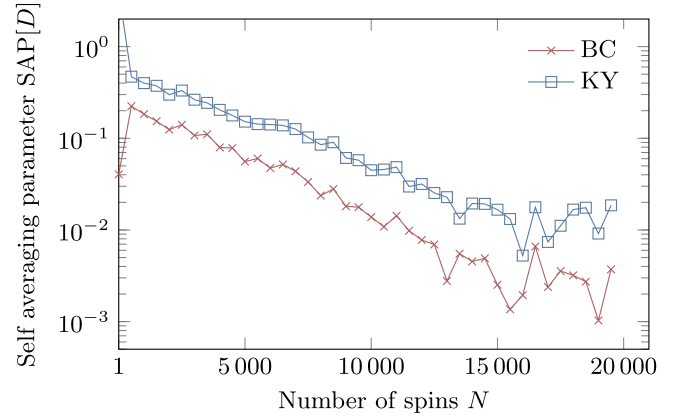


FIG. 14. The self-averaging parameter of the box counting and Kaplan-Yorke dimension in dependence on the number of spins appears to decrease exponentially to zero. Therefore the system shows self-averaging with respect to these dynamical properties for $C = 3.5$.

character vanishes. Note that the Kaplan-Yorke dimension should be lower than the box-counting according to the theory of the dimensions of chaotic attractors [64], which is also fully reflected by our simulations. Nevertheless the question remains whether the variance of the fractal dimension of the chaotic attractor vanishes for a large number of spins. To answer this question, we take a look at the coefficient of variation, also often called Self-Averaging Parameter (SAP) [65], of the fractal dimension D of the attractor, which is given by

$$SAP[D] = \frac{\overline{D^2} - \bar{D}^2}{\bar{D}^2}. \quad (35)$$

Here, as before, the bar \bar{X} denotes an average of X over different realization of the quenched local disorder. The SAP of the dimension was calculated for 500 disorder realizations $\{b_i\}$ and a varying number of spins N and is presented in a semi-log plot in Fig. 14. We find, that the SAP approaches zero also roughly exponentially for $N \rightarrow \infty$; hence, the system shows self-averaging with respect to the box counting and the Kaplan-Yorke dimension of the attractors. This means that for a small number of spins the fractal dimension strongly depends on the realization of the local disorder, whereas for a large number of spins, this dependence vanishes. Thus, fractal dimensions are self-averaging quantities and can be calculated from one typical disorder realization of a large system.

E. Magnetization

Besides the investigation of the dynamic properties of the system, the behavior of the magnetization of the RFIM shows some interesting behavior. We numerically calculated the variance of the magnetization

$$\text{VAR}[M] = \overline{\left(\frac{1}{N} \sum_i \langle \sigma_i \rangle\right)^2} - \bar{M}^2 \quad (36)$$

over 500 disorder realizations for two typical chaotic attractors with $C = 2.9$ and $C = 3.5$. Here $\langle \sigma_i \rangle$ denotes the

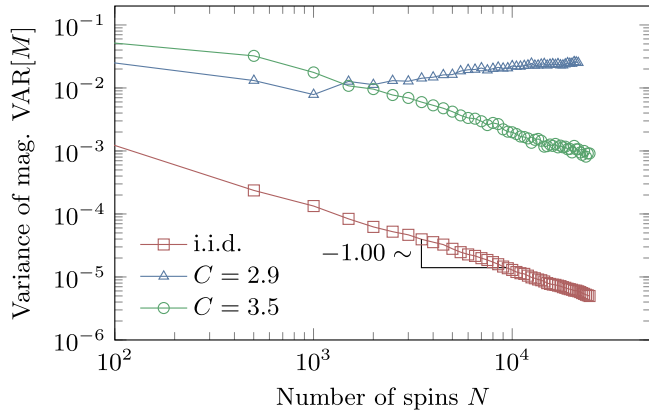


FIG. 15. For the attractor at $C = 3.5$ the variance of the magnetization goes algebraically to zero with N^{-1} for increasing number of spins similar to Independent and Identically Distributed (iid) input of the RFIM. In contrast, for $C = 2.9$ the variance does not vanish for a large number of spins.

time-average of the configuration of the i th spin and \bar{M} denotes the average of the magnetization of the system over the disorder realizations. In our case due to the symmetry in the distribution of the disorder with respect to the oscillator equilibrium, we have $\bar{M} = 0$. The resulting variance is presented in Fig. 15. We found that for the attractor at $C = 3.5$ the variance vanishes for an increasing number of spins (green circles). This is similar to the behavior, which can be found for independent and identically distributed input of the RFIM (red squares), which decreases algebraically to zero with N^{-1} ; this is fully in accordance to the expected behavior of the variance within the central limit theorem. In contrast, the magnetization does not show self-averaging for the attractor at $C = 2.9$ (blue triangles). In this case, the variance does not vanish for a large number of spins. The reason for that can be explained as follows. For $C = 2.9$, in general, many different attractors show up, and it depends on the specific disorder realization, which asymptotic state is reached by the system. For an increasing number of spins the system mainly ends up in one of two symmetric attractors, which are illustrated in Fig. 16 for $N = 20\,000$. The time average of the magnetization for the blue attractor (\blacksquare) is greater than zero, while the time

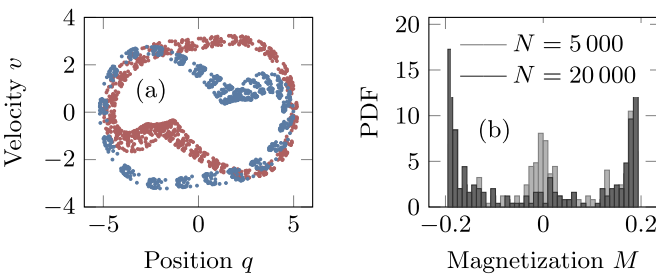


FIG. 16. (a): For $C = 2.9$ and $N = 20\,000$ there exist two different typical attractors of the system illustrated by the red (\blacksquare) and blue (\blacksquare) dots. This explains the non-self-averaging behavior of the magnetization. (b): The non-self-averaging behavior of the magnetization is also reflected in the corresponding histogram by the two main bars at $M = \pm 0.2$.

average of the red attractor (\blacksquare) is smaller than zero. The distribution of the magnetization is roughly symmetric and has two maxima at the positive and negative magnetization corresponding to the blue and red attractors (see Fig. 16). As a consequence, the variance of the magnetization does not go to zero even for a large number of spins and, in general, depends on the actual dynamics of the system.

V. CONCLUSION

Motivated by the phenomenon of complex hysteresis in many dynamical systems, we studied the exemplary system of a harmonic oscillator coupled to a simplified RFIM, where the input and output of the RFIM is the oscillator position and the magnetic force from the RFIM, respectively. We focused on the piecewise-smooth character of the system and neglected spin-spin interactions in the RFIM. In this case, each spin flips at a fixed oscillator position, which is determined by the local disorder parameter of the spins. These positions correspond to parallel boundaries in the phase space. At the boundaries the magnetic force jumps, whereas between the boundaries the force remains constant and the system is smooth.

The dynamics of the system with only a small number of spins is dominated by different grazing bifurcation scenarios, which are typical for piecewise-smooth systems. Chaotic solutions and multistability can be found already for the oscillator coupled to only one spin. For a large number of spins, the grazing bifurcation scenarios vanish, and the dynamic behavior of the piecewise-smooth system is very similar to the dynamic behavior of the smooth system in the thermodynamic limit with infinitely many spins. This is not obvious because the number of discontinuities increases. However, on the other hand the changes of the magnetization per spin flip decrease. As a result, the system becomes smoother, and in the thermodynamic limit the system can be described by a harmonic oscillator with a smooth nonlinear magnetic force. The smooth system is also able to show chaos. The typical box counting and the typical Kaplan-Yorke dimension of the chaotic attractors of the piecewise-smooth system converge to the corresponding dimensions of the smooth system in its thermodynamic limit. The variance of the attractor dimension vanishes for an increasing number of spins. This does not hold for the magnetization because there is a bistability between two symmetric attractors with a positive or negative average magnetization.

In future work we will focus on the case which includes spin-spin interactions. In this case hysteresis is possible in the RFIM, that is, the internal state of the RFIM is not necessarily determined only by the instantaneous oscillator position but also by past values of the input. This means that the system can still be treated as a piecewise-smooth dynamical system, but the boundaries in phase space, which are associated with the discontinuities due to a spin flip, are no longer fixed but become a history-dependent dynamic quantity.

ACKNOWLEDGMENT

We would like to thank Sven Schubert for helpful discussions and valuable suggestions.

- [1] A. Brinkman, M. Huijben, M. van Zalk, J. Huijben, U. Zeitler, J. C. Maan, W. G. van der Wiel, G. Rijnders, D. H. A. Blank, and H. Hilgenkamp, Magnetic effects at the interface between non-magnetic oxides, *Nat. Mater.* **6**, 493 (2007).
- [2] C. Song, J. Brandon, and C. A. Featherston, Distributed-element Preisach model for hysteresis of shape memory alloys, *J. Mech. Eng. Sci.* **215**, 673 (2001).
- [3] D. J. Late, B. Liu, H. S. S. R. Matte, V. P. Dravid, and C. N. R. Rao, Hysteresis in single-layer MoS₂ field effect transistors, *ACS Nano* **6**, 5635 (2012).
- [4] I. Urbanaviciute, T. D. Cornelissen, X. Meng, R. P. Sijbesma, and M. Kemerink, Physical reality of the Preisach model for organic ferroelectrics, *Nat. Commun.* **9**, 4409 (2018).
- [5] S. Horike, S. Shimomura, and S. Kitagawa, Soft porous crystals, *Nat. Chem.* **1**, 695 (2009).
- [6] S. Eckel, J. G. Lee, F. Jendrzejewski, N. Murray, C. W. Clark, C. J. Lobb, W. D. Phillips, M. Edwards, and G. K. Campbell, Hysteresis in a quantized superfluid ‘atomtronic’ circuit, *Nature (London)* **506**, 200 (2014).
- [7] P. Crespo, R. Litrán, T. C. Rojas, M. Multigner, J. M. de la Fuente, J. C. Sánchez-López, M. A. García, A. Hernando, S. Penadés, and A. Fernández, Permanent Magnetism, Magnetic Anisotropy, and Hysteresis of Thiol-Capped Gold Nanoparticles, *Phys. Rev. Lett.* **93**, 087204 (2004).
- [8] G. Bertotti and I. D. Mayergoyz, *The Science of Hysteresis*, 3 Vols. (Academic Press, New York, 2006).
- [9] F. Preisach, Über die magnetische Nachwirkung, *Z. Phys.* **94**, 277 (1935).
- [10] P. Weiss, Molecular field and ferromagnetic property: L’hypothèse du champ moléculaire et la propriété ferromagnétique, *J. Phys. Theor. Appl.* **6**, 661 (1907).
- [11] R. Peierls, On Ising’s model of ferromagnetism, *Math. Proc. Camb. Phil. Soc.* **32**, 477 (1936).
- [12] Y. Imry and S. Ma, Random-Field Instability of the Ordered State of Continuous Symmetry, *Phys. Rev. Lett.* **35**, 1399 (1975).
- [13] J. P. Sethna, K. Dahmen, S. Kartha, J. A. Krumhansl, B. W. Roberts, and J. D. Shore, Hysteresis and Hierarchies: Dynamics of Disorder-Driven First-Order Phase Transformations, *Phys. Rev. Lett.* **70**, 3347 (1993).
- [14] T. G. Sorop, C. Untiedt, F. Luis, M. Kroll, M. Rasa, and L. J. de Jongh, Magnetization reversal of ferromagnetic nanowires studied by magnetic force microscopy, *Phys. Rev. B* **67**, 014402 (2003).
- [15] J. Ortín, Preisach modeling of hysteresis for a pseudoelastic Cu-Zn-Al single crystal, *J. Appl. Phys.* **71**, 1454 (1992).
- [16] M. P. Lilly, A. H. Wootters, and R. B. Hallock, Spatially Extended Avalanches in a Hysteretic Capillary Condensation System: Superfluid ⁴He in Nuclepore, *Phys. Rev. Lett.* **77**, 4222 (1996).
- [17] O. Perkovic, K. A. Dahmen, and J. P. Sethna, Avalanches, Barkhausen Noise, and Plain Old Criticality, *Phys. Rev. Lett.* **75**, 4528 (1995).
- [18] T. Nattermann, Theory of the random field Ising model, in *Spin Glasses and Random Fields*, Series on Directions in Condensed Matter Physics, edited by A. P. Young (World Scientific, New Jersey, 1997), Vol. 12, pp. 277–298.
- [19] P. Shukla, Exact solution of return hysteresis loops in a one-dimensional random-field Ising model at zero temperature, *Phys. Rev. E* **62**, 4725 (2000).
- [20] J. P. Sethna, K. A. Dahmen, and C. R. Myers, Crackling noise, *Nature (London)* **410**, 242 (2001).
- [21] I. D. Mayergoyz and C. E. Korman, The Preisach model with stochastic input as a model for aftereffect, *J. Appl. Phys.* **75**, 5478 (1994).
- [22] P. Rugkwamsook, C. E. Korman, G. Bertotti, and M. Pasquale, Dependence of aftereffect on magnetization history, *J. Appl. Phys.* **85**, 4361 (1999).
- [23] M. Dimian and I. D. Mayergoyz, Spectral density analysis of nonlinear hysteretic systems, *Phys. Rev. E* **70**, 046124 (2004).
- [24] A. Adedoyin, M. Dimian, and P. Andrei, Analysis of noise spectral density for phenomenological models of hysteresis, *IEEE Trans. Magn.* **45**, 3934 (2009).
- [25] G. Radons, Spectral properties of the Preisach hysteresis model with random input. I. General results, *Phys. Rev. E* **77**, 061133 (2008).
- [26] G. Radons, Spectral properties of the Preisach hysteresis model with random input. II. Universality classes for symmetric elementary loops, *Phys. Rev. E* **77**, 061134 (2008).
- [27] G. Radons, Hysteresis-Induced Long-Time Tails, *Phys. Rev. Lett.* **100**, 240602 (2008).
- [28] S. Schubert and G. Radons, Preisach models of hysteresis driven by Markovian input processes, *Phys. Rev. E* **96**, 022117 (2017).
- [29] H. Lamba, M. Grinfeld, S. McKee, and R. Simpson, Subharmonic ferroresonance in an LCR circuit with hysteresis, *IEEE Trans. Magn.* **33**, 2495 (1997).
- [30] A. Rezaei-Zare, M. Sanaye-Pasand, H. Mohseni, S. Farhangi, and R. Irvani, Analysis of ferroresonance modes in power transformers using Preisach-type hysteretic magnetizing inductance, *IEEE Trans. Power Delivery* **22**, 919 (2007).
- [31] G. Radons and A. Zienert, Nonlinear dynamics of complex hysteretic systems: Oscillator in a magnetic field, *Eur. Phys. J. Special Topics* **222**, 1675 (2013).
- [32] P. A. Cook, Simple feedback systems with chaotic behaviour, *Syst. Control Lett.* **6**, 223 (1985).
- [33] K. H. Johansson, A. Rantzer, and K. H. Åström, Fast switches in relay feedback systems, *Automatica* **35**, 539 (1999).
- [34] J. M. Goncalves, A. Megretski, and M. A. Dahleh, Global stability of relay feedback systems, *IEEE Trans. Automatic Control* **46**, 550 (2001).
- [35] M. Wiercigroch, R. D. Neilson, and M. A. Player, Material removal rate prediction for ultrasonic drilling of hard materials using an impact oscillator approach, *Phys. Lett. A* **259**, 91 (1999).
- [36] S. Theodossiades and S. Natsiavas, Non-linear dynamics of gear-pair systems with periodic stiffness and backlash, *J. Sound Vib.* **229**, 287 (2000).
- [37] K. Popp and P. Shelter, Stick-slip vibrations and chaos, *Philos. Trans.: Phys. Sci. Eng.* **332**, 89 (1990).
- [38] U. Galvanetto, Some discontinuous bifurcations in a two-blocks stick-slip system, *J. Sound Vib.* **248**, 653 (2001).
- [39] M. di Bernardo, C. Budd, A. R. Champneys, and P. Kowalczyk, *Piecewise-Smooth Dynamical Systems: Theory and Applications*, Applied Mathematical Sciences (Springer, London, 2008), Vol. 163.
- [40] M. S. Santina and A. R. Stubberud, Basics of sampling and quantization, in *Handbook of Networked and Embedded Control Systems*, edited by D. Hristu-Varsakelis and W. S. Levine (Birkhäuser, Boston, 2005), pp. 45–69.

- [41] E. Vives, M. L. Rosinberg, and G. Tarjus, Hysteresis and avalanches in the $t = 0$ random-field Ising model with two-spin-flip dynamics, *Phys. Rev. B* **71**, 134424 (2005).
- [42] F. Salvat-Pujol, E. Vives, and M. L. Rosinberg, Hysteresis in the $t = 0$ random-field Ising model: Beyond metastable dynamics, *Phys. Rev. E* **79**, 061116 (2009).
- [43] A. A. Middleton, Asymptotic Uniqueness of the Sliding State for Charge-Density Waves, *Phys. Rev. Lett.* **68**, 670 (1992).
- [44] D. Dhar, P. Shukla, and J. P. Sethna, Zero-temperature hysteresis in the random-field Ising model on a Bethe lattice, *J. Phys. A: Math. Gen.* **30**, 5259 (1997).
- [45] A. V. Goldberg and R. E. Tarjan, A new approach to the maximum-flow problem, *J. ACM* **35**, 921 (1988).
- [46] A. K. Hartmann and K. D. Usadel, Exact determination of all ground states of random field systems in polynomial time, *Physica A* **214**, 141 (1995).
- [47] A. A. Middleton, Critical Slowing Down in Polynomial Time Algorithms, *Phys. Rev. Lett.* **88**, 017202 (2001).
- [48] I. Dukovski and J. Machta, Ground-state numerical study of the three-dimensional random-field Ising model, *Phys. Rev. B* **67**, 014413 (2003).
- [49] P. E. Theodorakis and N. G. Fytas, Random-field Ising model: Insight from zero-temperature simulations, *Condens. Matter Phys.* **17**, 43003 (2014).
- [50] U. Wolff, Collective Monte Carlo Updating for Spin Systems, *Phys. Rev. Lett.* **62**, 361 (1989).
- [51] A. K. Hartmann, Cluster-exact approximation of spin glass groundstates, *Physica A* **224**, 480 (1996).
- [52] M. C. Kuntz, O. Perkovic, K. A. Dahmen, B. W. Roberts, and J. P. Sethna, Hysteresis, avalanches, and noise: Numerical methods, *Comput. Sci. Eng.* **1**, 73 (1999).
- [53] G. Benettin, L. Galgani, A. Giorgilli, and J. Strelcyn, Lyapunov characteristic exponents for smooth dynamical systems and for Hamiltonian systems; a method for computing all of them. Part 1: Theory. Part 2: Numerical applications, *Meccanica* **15**, 9 (1980).
- [54] A. B. Nordmark, Non-periodic motion caused by grazing incidence in an impact oscillator, *J. Sound Vib.* **145**, 279 (1991).
- [55] P. C. Müller, Calculation of Lyapunov exponents for dynamic systems with discontinuities, *Chaos Solitons Fractals* **5**, 1671 (1995).
- [56] H. Dankowicz and A. B. Nordmark, On the origin and bifurcations of stick-slip oscillations, *Physica D* **136**, 280 (2000).
- [57] M. di Bernardo, C. J. Budd, and A. R. Champneys, Grazing and Border-Collision in Piecewise-Smooth Systems: A Unified Analytical Framework, *Phys. Rev. Lett.* **86**, 2553 (2001).
- [58] M. di Bernardo, C. J. Budd, and A. R. Champneys, Normal form maps for grazing bifurcations in n -dimensional piecewise-smooth dynamical systems, *Physica D* **160**, 222 (2001).
- [59] C. Budd and F. Dux, Intermittency in impact oscillators close to resonance, *Nonlinearity* **7**, 1191 (1994).
- [60] W. Chin, E. Ott, H. E. Nusse, and C. Grebogi, Grazing bifurcations in impact oscillators, *Phys. Rev. E* **50**, 4427 (1994).
- [61] S. Foale and S. R. Bishop, Bifurcations in impact oscillations, *Nonlinear Dyn.* **6**, 285 (1994).
- [62] H. G. E. Hentschel and I. Procaccia, The infinite number of generalized dimensions of fractals and strange attractors, *Physica D* **8**, 435 (1983).
- [63] P. Grassberger and I. Procaccia, Measuring the strangeness of strange attractors, *Physica D* **9**, 189 (1983).
- [64] J. D. Farmer, E. Ott, and J. A. Yorke, The dimension of chaotic attractors, *Physica D* **7**, 153 (1983).
- [65] A. Aharony and A. B. Harris, Absence of Self-Averaging and Universal Fluctuations in Random Systems Near Critical Points, *Phys. Rev. Lett.* **77**, 3700 (1996).